Miner Petrol (2013) 107:415–428
DOI 10.1007/s00710-013-0286-2

ORIGINAL PAPER

Factors affecting the Nd^{3+} (REE^{3+}) luminescence of minerals

Christoph Lenz · Dominik Talla · Katja Ruschel · Radek Škoda · Jens Götze · Lutz Nasdala

Received: 12 November 2012 / Accepted: 14 April 2013 / Published online: 8 May 2013

Abstract In this paper, possibilities and limits of the application of REE^{3+} luminescence (especially the Nd^{3+} $^4F_{3/2} \rightarrow {}^4I_{9/2}$ emission) as structural probe are evaluated. Important factors controlling the Nd^{3+} luminescence signal are discussed, including effects of the crystal-field, crystal orientation, structural state, and temperature. Particular attention was paid to the study of the accessory minerals zircon ($ZrSiO_4$), xenotime–(Y) (YPO_4), monazite–(Ce) ($CePO_4$) and their synthetic analogues. Based on these examples we review in short that (1) REE^{3+} luminescence can be used as non-destructive phase identification method, (2) the intensities of certain luminescence bands are strongly influenced by crystal orientation effects, and (3) increased widths of REE^{3+}-related emission bands are a strong indicator for structural disorder. We discuss the potential of luminescence spectroscopy, complementary to Raman spectroscopy, for the quantitative estimation of chemical (and potentially also radiation-induced) disorder. For the latter, emissions of Nd^{3+}-related centres are found to be promising candidates.

Editorial handling: J. M. Hanchar and A. Beran

C. Lenz (✉) · D. Talla · K. Ruschel · L. Nasdala
Institut für Mineralogie und Kristallographie, Universität Wien, Althanstraße 14, 1090 Wien, Austria
e-mail: christoph.lenz@univie.ac.at

D. Talla · R. Škoda
Institute of Geological Sciences, Masaryk University, Kotlářská 2, 61137 Brno, Czech Republic

J. Götze
Institut für Mineralogie, TU Bergakademie Freiberg, Brennhausgasse 14, 09596 Freiberg, Germany

Introduction

The luminescence emission of rare-earth elements (REEs) in general is well-studied, stimulated by their importance in various modern technological applications such as lighting, colour-television screens, solid-state lasers, phosphors, and chromophores in different host materials (e.g., Belsky and Krupa 1999; Kenyon 2002; Bünzli and Piguet 2005; Liu and Jacquier 2005). In the Earth sciences, one challenging task is the detection of REEs in different host minerals using luminescence methods; a large variety of mineral systems have been studied already (Tarashchan 1978; Ohnenstetter et al. 1991; Habermann et al. 1996; Gaft et al. 1999; Götze et al. 1999; Blanc et al. 2000; Waychunas 2002; Nasdala et al. 2004; Gaft et al. 2005; Czaja et al. 2008). Synthetic minerals individually- or multi-doped with REEs have also been studied routinely, aiming at a better understanding of the luminescence in their natural analogues. For the example of zircon and synthetic $ZrSiO_4$, such investigations have been done by Cesbron et al. (1993, 1995), Blanc et al. (2000), Hanchar et al. (2001), and Friis et al. (2009). Time-resolved luminescence techniques have improved the detection of various luminescence centres utilizing their different decay times (Reisfeld et al. 1996; Gaft et al. 1999; Gaft et al. 2001). Furthermore, unravelling the internal zoning of the REE distribution within crystals, especially of accessory minerals, may provide valuable information on their primary formation and post-growth history. Such patterns are visualised easily using luminescence techniques (Hanchar and Miller 1993; Hanchar and Rudnick 1995; Rakovan and Reeder 1996; Götze 2000, 2002; see also the review chapter by Götze et al. in this special issue).

In addition to traditional direct imaging, the luminescence of crystals and other geological samples is studied increasingly using (hyperspectral) mapping techniques (see the review

chapter by MacRae et al. in this special issue). The need four sound spectral interpretation in reducing such hyperspectral data sets has increased the interest in a detailed understanding of REE luminescence features (Nasdala et al. 2004; MacRae et al. 2005). For a number of minerals, luminescence-intensity based quantifications of trace REEs have been proposed (Barbarand and Pagel 2001; Habermann 2002; Richter et al. 2003; MacRae et al. 2005; 2012). Moreover, traces of REE^{3+} in minerals and mineral-based ceramics are used as structural probes studied with respect to order–disorder phenomena, in particular the accumulation of structural damage as caused by irradiation. For instance, spectral parameters of Eu^{3+} emissions have been used for the characterisation of REE-substituted cation-sites in glasses and crystalline materials in process of evaluation of potential nuclear waste forms (Ollier et al. 2003; Reisfeld et al. 2004; Reisfeld 2005; Ternane et al. 2005). Seydoux-Guillaume et al. (2002) and Panczer et al. (2012) proposed that the REE-dominated luminescence emission of monazite–(Ce) may bear quantitative information on the accumulated radiation-damage in this mineral.

In accordance to the finding of the latter authors, we consider the luminescence signal of Nd^{3+} as particularly promising structural probe. The $^4F_{3/2} \rightarrow {}^4I_{9/2}$ electronic transition of Nd^{3+} causes luminescence emission in the near-infrared (NIR) spectral range between 10,600 and 11,800 cm^{-1} (830–940 nm). This emission is a promising candidate because : (1) the luminescence signal can be collected with standard Si-based detectors; (2) it is effectively excited by standard lasers, e.g., Ar^+ (488 nm, 514 nm) as well as via accelerated electrons (cathodoluminescence, CL); (3) other luminescence emissions in the respective wavenumber range are rare; and (4) it has been identified in many mineral hosts, especially in REE-bearing accessory minerals. The application of Nd^{3+} (REE^{3+}) luminescence as a structural probe requires a detailed understanding of the influencing factors and their calibration, respectively. Here we discuss the basic effects of (1) the crystal field environment; (2) crystal orientation; (3) structural disorder; and (4) temperature on the Nd^{3+} luminescence as representative example. Similar to Nd^{3+}, other appropriate REE^{3+} can be used, e.g., Pr^{3+}, Sm^{3+}, Eu^{3+}, but are not discussed in this work. In this study, the Nd^{3+} hosts zircon, xenotime–(Y) and monazite–(Ce) and their synthetic analogues have been studied in detail.

Samples & methods

Samples and preparation

Luminescence investigations were performed on a large variety of specimens including monazite–(Ce), Zircon and xenotime–(Y) and/or their synthetic analogues (see Table 1). An overview of the chemically homogeneous, natural monazite–(Ce) samples measured here, including their origins and ages, is given in Ruschel et al. (2012). Only samples of these authors that were annealed in air to reconstitute their crystalline state were chosen for the study of chemical-induced disorder, to avoid biases of the results due to effects of self-irradiation damage on the luminescence parameters obtained. In addition, a range of flux-grown, synthetic samples were studied, including $Ce_{1-x}LREE_xPO_4$ (with LREE = La, Nd, Gd) of Ruschel et al. (2012) and $CePO_4$ samples with predominant *cheralite* ($2\ REE^{3+} \leftrightarrow Ca^{2+} + Th^{4+}$) or *huttonite* ($P^{5+} + REE^{3+} \leftrightarrow Si^{4+} + Th^{4+}$) substitution (synthesised in this study; see below).

The orientation-dependence of the luminescence was studied for Nd-doped YPO_4 samples synthesised by Talla et al. (2011), and Nd-doped $ZrSiO_4$ crystals produced in this study (see sub-chapter "Details on synthesis procedures" below). An overview of the samples investigated is given in Table 1.

Doubly polished thin sections (thicknesses ~30 μm) attached to a glass slide were prepared with respect to the crystallographic orientation (xenotime and zircon samples),

Table 1 Overview of samples studied in detail

Samples		Substitution type	Reference
Monazite-(Ce)	natural	huttonite + cheralite	all homogeneous, dry-annealed monazite–(Ce) samples from Ruschel et al. (2012)
	synthetic	$Ce_{1-x}REE_x[PO_4]$ substitution	Nd-, Gd- and/or La-containing homogeneous samples from Ruschel et al. (2012)
	synthetic	cheralite + "Na-Th substitution" $Ce_{1-x-y}\ Ca_{0.5x}Na_{y/3}Th_{0.5+2y/3}[PO_4]$	this study; see in "Details on synthesis procedures"
Zircon	synthetic	almost pure crystals doped with trace Nd^{3+} without charge compensation	this study; see in "Details on synthesis procedures"
	synthetic	almost pure crystals doped with trace Nd^{3+} incorporated via xenotime substitution, $Zr_{1-x}Nd_x[Si_{1-x}P_xO_4]$	this study; see in "Details on synthesis procedures"
Xenotime-(Y)	synthetic	crystals doped with Nd^{3+} incorporated via $Y_{1-x}Nd_x[PO_4]$ substitution	Talla et al. (2011)

or as randomly cut slabs (monazite samples from Ruschel et al. 2012). For electron microprobe and cathodoluminescence analysis the sections were coated with carbon.

Details on synthesis procedures

Synthetic monazite–(Ce) crystals with predominant cheralite or huttonite substitution were produced by a flux method using the slow-cooling technique. Sodium polyphosphate was preferentially used as flux material because of its good solubility in water, making the extraction of the resulting product straightforward (and fast in comparison with $Pb_2P_2O_7$, commonly used for REE phosphate syntheses; Boatner 2002; Talla et al. 2011). Platinum crucibles with a volume of 100 cm^3 were used as reaction vessels. For each batch, 10 grams of $NaPO_3$ were used as flux material and mixed with $CeCl_3.7H_2O$, setting the molar ratio Ce/(Ce+Na) in the melt to 0.12 (Talla et al. 2011). A total of five samples of Th-doped monazite–(Ce) were produced using $Th(NO_3)_4.5H_2O$. In the first three, Th was added in varying amounts, the weight ratio Th/(Th+Ce) in the melt being 400, 2,000 and 10,000 ppm. Charge balance was provided using the *cheralite substitution* mechanism ($2\ REE^{3+} \leftrightarrow Ca^{2+} + Th^{4+}$) with $CaCO_3$ (analytical grade) as source of Ca. A fourth, un-doped sample was also produced for comparison (blank). In the fifth sample, the *huttonite substitution* ($P^{5+} + REE^{3+} \leftrightarrow Si^{4+} + Th^{4+}$) was used as the mechanism for introducing Th into monazite–(Ce) with silica as source of Si. The weight fraction Si/(Si+Ce+Th) in the melt was adjusted to 0.02. All reagents were of analytical grade except for $NaPO_3$ and the cerium chloride. Preliminary tests showed that pollutant trace Nd present in the commercial $CeCl_3.7H_2O$ results in minute concentrations of Nd in the $CePO_4$ samples grown, which, however, yield easily measurable Nd^{3+}-luminescence emissions. A separate Nd source was therefore not added to the crucible. After being filled, the Pt crucibles were capped by a loose lid. Crucibles were first heated to a peak temperature of 1,170 °C, at a rate of 230 K per hour. This temperature was kept for 2 hours, and reduced afterwards to 900 °C, at a rate of −1.35 K per hour. The furnace was then switched off, and it was not opened until samples had cooled down slowly to room temperature. The crystals produced were about 0.3–1.0 mm in size. Their colours range from light green (low-Th syntheses) to colourless (elevated Th content). The total amount of crystals produced was much smaller when higher concentrations of heterovalent substituents were present. A detailed microchemical characterisation of these synthetic samples is given in Table 2.

Synthesis of zircon crystals (up to 1.5 mm) was accomplished by a flux technique similar to that described by Cesbron et al. (1993, 1995) and Hanchar et al. (2001) with an adjusted synthesis route combining the evaporation of the highly volatile MoO_3 with a rapid cooling rate. This allowed us to use an alkali-free mixture of 0.53 g ZrO_2 with 0.26 g SiO_2 and 10 g MoO_3, preventing the incorporation of Li^+ into the zircon crystals (Hanchar et al. 2001). Preliminary test runs showed that the resulting ratios of 0.07 mol% (Zr+Si)/(Zr+Si+Mo) and 1:1 Zr/Si resulted in the growth of larger, well-developed crystals. To produce Nd-doped $ZrSiO_4$, a minor amount of Nd was added. This was done in two different ways, first by adding Nd_2O_3 without any additional charge-

Table 2 Chemical formulae of synthetic Th-doped monazite-(Ce) samples in atomic percent per formula unit (apfu), calculated from average electron-microprobe data of different chemically heterogeneous zones. The distortional behaviour of all substituents (Δ) and heterovalent substituents (Δ_{hetero}) are approximated with a weighted ionic radii difference between the predominant cation/anion [Ce/P in monazite–(Ce)] and each substituent (see Eq. 1)

		Chemical formula (apfu)									
Sample	Point	Ce	Nd	Na	Ca	Th	U	P	Si	Δ	Δ_{hetero}
C1 *(blank)*	1	0.999	0.001	bdl	bdl	bdl	bdl	0.999	bdl	0.00012	0.00009
C2	2	0.998	0.001	bdl	0.001	bdl	bdl	0.999	bdl	0.00011	0.00008
C3	3	0.997	0.002	bdl	bdl	bdl	bdl	0.999	bdl	0.00015	0.00008
	4	0.939	0.001	0.010	0.013	0.037	0.001	0.997	bdl	0.00405	0.00023
	5	0.941	0.001	0.009	0.014	0.036	0.001	0.999	bdl	0.00377	0.00374
	6	0.915	0.001	0.015	0.018	0.051	0.001	0.999	bdl	0.00522	0.00520
C4	7	0.864	0.001	0.023	0.029	0.083	0.001	0.999	bdl	0.00850	0.00847
	8	0.931	0.001	0.012	0.015	0.040	0.001	1.000	bdl	0.00410	0.00407
	9	0.997	0.001	0.001	0.001	bdl	bdl	0.999	bdl	0.00010	0.00004
CSi	10	0.987	0.012	bdl	bdl	0.001	bdl	1.000	bdl	0.00044	0.00002
	11	0.960	bdl	0.010	0.001	0.001	bdl	0.999	bdl	0.00266	0.00264
	12	0.867	bdl	0.040	0.002	0.089	0.001	0.999	bdl	0.00805	0.00803
	13	0.909	bdl	0.027	0.002	0.061	bdl	0.999	0.001	0.00556	0.00554

compensating species, and second by adding $NdPO_4$ ensuring charge balance via the *xenotime substitution* ($Zr^{4+} + Si^{4+} \leftrightarrow REE^{3+} + P^{5+}$). The molar ratio Nd/(Nd+Zr) in the melt was adjusted to 0.6 mol%. The temperature path consisted of heating the loosely capped Pt crucibles to 1,100 °C, at a rate of 216 K per hour. Without a soaking interval, the temperature was then reduced to 700 °C, at a rate of −26.5 K per hour. Afterwards, samples were left in the furnace to cool slowly. Crystals were extracted manually (i.e., without the need to use any chemical reagents) from the crucible without problems. It was found that the size of the crystals grown was influenced strongly by the evaporation surface of the melt during the experiment. A small evaporation surface prevents rapid vaporisation of Mo-flux, the solvent of all reagents. Therefore, thinner crucibles result in the formation of larger single-crystals.

Analytical methods

Electron microprobe analyses were performed using a Cameca SX100 electron microprobe with the following measurement conditions: accelerating voltage 15 kV, beam current 20 nA, and 8 μm beam diameter. A defocused beam was in order to minimize the loss of Na during analysis. The peak counting times were 20 s for major elements and 40 to 60 s for minor and trace elements; counting times for the background (measured on both, the high- and low-energy side) were set to half of the respective peak counting-time. The following natural and synthetic standards were used: $Si_{K\alpha}$-natural sanidine, Eifel; $Na_{K\alpha}$-natural albite, Amelia; $P_{K\alpha}$-$LaPO_4$; $Ca_{K\alpha}$,$Th_{M\alpha}$-synthetic $CaTh(PO_4)_2$; $Ce_{L\alpha}$-synthetic $CePO_4$; $Nd_{L\beta}$-synthetic $NdPO_4$; $U_{M\beta}$-synthetic U. The raw data were corrected using the PAP routine (Pouchou and Pichoir 1991). Elemental X-ray maps were acquired at following conditions: accelerating voltage 15 kV, beam current 60 nA, and <1 μm beam diameter. Signals of $Na_{K\alpha}$, $P_{K\alpha}$, $Ce_{L\alpha}$, $Nd_{L\beta}$, and $Th_{M\alpha}$, and backgrounds for each element were collected. The data were acquired in stage moving mode, with 1 μm step width and 50 ms dwell time. The collected peak intensities were corrected for the background intensities and converted to absolute concentrations. Finally colour-coded element distribution maps were produced to visualize internal distribution patterns for certain chemical components.

Cathodoluminescence (CL) spectroscopy was performed using a hot cathode luminescence microscope (HC1-LM) with a high-vacuum chamber (< 10^{-6} bar). Spectral acquisition was done with an Acton Spectra Pro 2300i spectrometer with a charge-coupled device (CCD) detector, which is attached to the CL microscope by a silica-glass fibre-guide. Measurements were taken with a 100 μm slit, a 150 s line grid, an accelerating voltage of 14 kV and a current of 0.2 mA with a current density of approximately 10 μA mm^{-2}. Calibration was done with the mercury vapour discharge emission. The optical aperture produces a spot size of 30 μm. Cathodoluminescence examinations were carried out on polished thin sections that are coated with carbon to prevent any build-up of electrical charge during CL operation (further details in Neuser et al. 1995).

Room-temperature laser-induced photoluminescence measurements were carried out by means of a Horiba Jobin Yvon LabRam-HR (high resolution) system equipped with an Olympus BX41 optical microscope, a grating with 600 grooves per millimetre, and a Si-based, Peltier-cooled CCD detector. Luminescence spectra were excited using the continuous 532 nm emission of a frequency-doubled Nd:YAG laser (34 mW on the sample surface). With the system operated in confocal mode and an Olympus 100× objective (numerical aperture=0.9), the lateral resolution was better than 1.5 μm, and the depth resolution (with the laser beam focused at the sample surface) was approximately 3 μm. The spectral resolution in the NIR was determined to be ~2 cm^{-1}. Wavenumber calibration was done using the Rayleigh line and Ne lamp emissions; the wavenumber accuracy was better than 0.5 cm^{-1}. Temperature-dependent measurements were done adding a Linkam FTIR 600 liquid-nitrogen cooling stage. The temperature accuracy was better than 2 K. Photoluminescence (hyperspectral) maps were obtained using a software-controlled x–y stage, with a step width of 3 μm.

Luminescence bands were fitted assuming Lorentzian-Gaussian (pseudo-Voigt) band shapes. Background correction turned out to be unnecessary.

Fingerprints of Nd^{3+} luminescence emission: generalities

Luminescence emissions are generated through the (radiative) release of energy during electronic transitions. Emission spectra of REE^{3+} in crystalline hosts are characterised by very sharp bands in contrast to the luminescence of 3*d* or 4*d* elements (Blasse and Grabmaier 1994). This unique characteristic of REE^{3+} luminescence is determined by their particular electron configuration. Trivalent rare earth ions (Ce^{3+} to Yb^{3+}) have an incompletely filled 4*f* shell which is shielded by outer filled $5s^2$ and $5p^6$ orbitals. In consequence, the influence from ligands in the host matrix is small (but of crucial importance). The narrow luminescence bands originate from intra-configurational $4f^n$ electronic transitions. The distinct $4f^n$ energy levels result from different electronic interactions. The four kinds of electronic interactions are illustrated in Fig. 1 for the example of Nd^{3+} with $4f^3$ electron configuration. The energetic state of $4f^n$ electrons in free REE^{3+} ions splits into spectroscopic *terms* due to the repulsion of unpaired 4*f* electrons (*electron–electron interaction*). In REE^{3+} ions, this term-splitting is on the order of ca. 10^4 cm^{-1} (Marfunin 1979). While the possible influence of negative charges from ligands is low, these terms further split into spectroscopic *levels* due to their *spin-orbit coupling* (on the order of ca. 10^3 cm^{-1}). Note that the separation of energy levels by these interactions applies to free REE^{3+} ions.

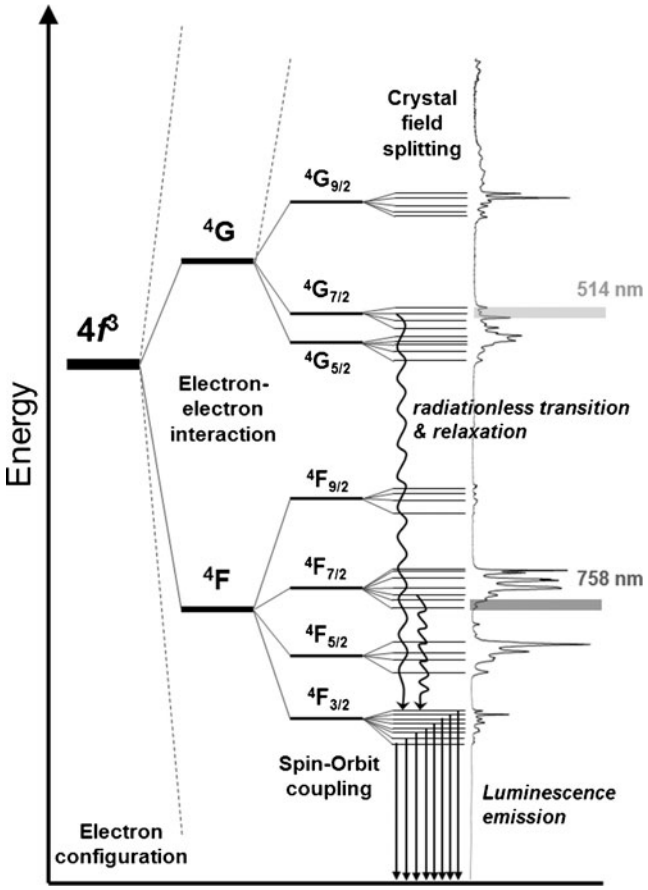

Fig. 1 Schematic illustration of the generation of electronic states for the example of Nd^{3+} with $4f^3$ electronic configuration. As examples for typical photoluminescence excitations, energies of photons of 514 and 758 nm laser light are marked on the right. After various excitation and subsequent relaxation processes, electrons eventually reach the lowest excited level ($^4F_{3/2}$). The transition from this level to the ground state is typically a radiative process that results in the emission of light, observed in the near-infrared range of the electromagnetic spectrum

An important result is that REE^{3+} optical transitions appear at similar energy ranges in very different host materials. A complete diagram of possible energy levels for each REE^{3+} is given in Carnall et al. (1989). If REE^{3+} ions are further surrounded by ligands e.g., in molecules (*ligand field*) or solids (*crystal field*), the electronic levels split into *sublevels* (*Stark level* splitting on the order of ca. 10^2 cm^{-1}; cf. Fig. 1). According to the *crystal field theory* (cf. Burns 1993) ligand-directed orbitals experience an energy destabilization due to repulsion with the negative charge of the ligand. Non-directed orbitals are stabilized, as their potential energy drops. The crystal field splitting depends on a variety of parameters connected to the site of the REE^{3+} within the crystal structure, e.g., site symmetry, the interatomic distance to the ligands, charge of ligands etc. Given the different characteristics of cation sites among minerals, REE^{3+} spectra may provide site-specific information on the short-range order.

Figure 2 exemplifies the Nd^{3+} photoluminescence of five different hosts: the accessory minerals xenotime–(Y), monazite–(Ce), titanite, and synthetic cubic zirconia (YCZ) and Yttrium-aluminium garnet (YAG). In all hosts the Nd^{3+}-related ($^4F_{3/2} \rightarrow {}^4I_{9/2}$) luminescence emission can be detected within the spectral range between 10,600 and 11,800 cm^{-1} (940–840 nm). Yttrium-stabilized zirconia (fluorite structure type, *Fm3m*) and YAG (garnet structure type, *Ia3d*) are well known synthetic gemstones, both with cubic symmetry. Xenotime–(Y) crystallizes in the tetragonal space group $I4_1/amd$. Monazite ($P2_1/n$) and titanite ($P2_1/a$) have monoclinic crystal structures. The completely different crystal field around the Nd^{3+}-centre is reflected by strongly differing photoluminescence spectra (Fig. 2). Note that in many minerals probably more than one substitutional REE-site exists (e.g., apatite, Czaja et al. 2009). In these cases standard steady-state luminescence techniques obtain the luminescence signal from all potential sites possibly differing from sample to sample. Time-resolved luminescence spectroscopy or site-selective spectroscopy may offer differentiation possibilities (Dexpert-Ghys et al. 1984; Dexpert-Ghys et al. 1996; Gaft et al. 1997; Piriou et al. 2001).

Comparing the isostructural minerals monazite–(Ce) ($CePO_4$) and gasparite–(Ce) ($CeAsO_4$), both with C_1 cation site symmetry, reveals a comparatively close Nd^{3+}-luminescence pattern with only minor band shifts (Fig. 3a). Note that the band width is strongly influenced by chemical heterogeneity and intensity ratios by the crystal orientation (in more detail discussed below).

The minerals xenotime–(Y) (YPO_4) and chernovite–(Y) ($YAsO_4$) are isostructural with zircon ($ZrSiO_4$). All crystallize in space group $I4_1/amd$ with D_{2d} cation site symmetry.

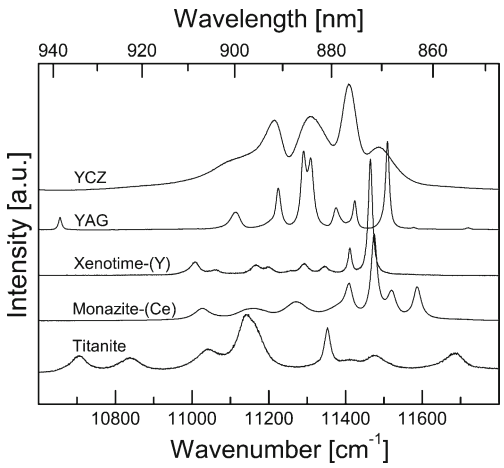

Fig. 2 Photoluminescence spectra (532 nm excitation) of Nd^{3+} ($^4F_{3/2} \rightarrow {}^4I_{9/2}$) in different host minerals: Yttrium-stabilized cubic zirconia (YCZ), yttrium-aluminium garnet (YAG), xenotime–(Y), monazite–(Ce), and titanite. Different cationic environments of the substituted Nd^{3+} cause dissimilar crystal field splittings and hence fingerprint-like luminescence patterns

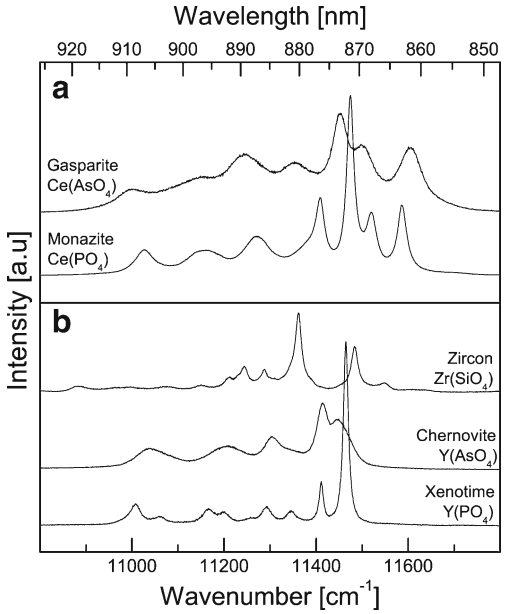

Fig. 3 Photoluminescence spectra (532 nm excitation) of Nd^{3+} ($^4F_{3/2} \rightarrow {}^4I_{9/2}$) in two groups of isostructural minerals. **a** Gasparite–(Ce) and monazite–(Ce) with cation site-symmetry C_1. **b** Zircon, chernovite–(Y), and xenotime–(Y) with cation site-symmetry D_{2d}

Whereas xenotime–(Y) and chernovite–(Y) show similarities in the Nd^{3+}-luminescence spectra, zircon differs remarkably, despite having the same site symmetry (Fig. 3b). Synthetic Nd^{3+}:$ZrSiO_4$ charge-balanced with P^{5+} and without, as well as reference zircons from various locations were compared; their Nd^{3+} luminescence shows a similar pattern to that of synthetic Nd^{3+}:$ZrSiO_4$ shown in Fig. 3b. This example demonstrates the impact of a modified *electronic* structure on the luminescence pattern: xenotime–(Y) and chernovite–(Y) have an isotypic crystal structure with chemically related elements; both have trivalent Y^{3+} on the cationic and $P^{5+}/As^{5+}O_4$ on the anionic position. Zircon is different, having tetravalent Zr^{4+} at the cation and $Si^{4+}O_4$ at the anion sites, respectively. A different charge distribution at the substitutional REE^{3+} site remarkably affects the crystal field splitting, and therefore the REE^{3+} luminescence signal.

Luminescence studies on synthetic mineral analogues provide both: (1) a better identification of a REE in a specific host since the luminescence signal of many REE^{3+} overlap and a discrimination is complicated in natural specimens (e.g., Sm^{3+}–Pr^{3+}); and (2) a fast mineral identification when the individual sublevel splitting is known, potentially applied to igneous/metamorphic or sedimentary petrology (Richter et al. 2008).

Orientation-dependence of REE^{3+} luminescence

As mentioned above, the crystal-field splitting depends on the site symmetry of the REE^{3+}-substituted cation site. A direct consequence is that the luminescence intensity of sublevels depends on the orientation of the measuring direction to certain symmetry elements of the crystal structure. Even though being a well-known luminescence phenomenon (Owen et al. 1998; Barbarand and Pagel 2001; Finch et al. 2003), the orientation-dependence of REE^{3+} emissions is often neglected, which may result in biased conclusions. To give two examples: Czaja et al. (2009) proposed to use the intensity ratio of emissions related to Pr^{3+} and Sm^{3+} to determine Pr/Sm ratios in apatite. Habermann (2002) applied REE-cathodoluminescence intensity for a semi-quantitative estimation of REE trace element concentration in calcite. In those papers, however, authors failed to consider possible luminescence intensity differences due to the orientation-dependence of the emissions analysed. For this reason, the orientation dependence of REE^{3+} luminescence on the example of Nd^{3+} is exemplified here for the sake of completeness (cf. Cesbron et al. 1995, Gaft et al. 2005).

Depending on the luminescence technique applied, different aspects of orientation effects can be discerned. In laser-induced photoluminescence studies the polarisation of the incident laser has to be considered, because most standard apparatus provide a strongly linear-polarised beam due to polarising effects of optical components (e.g., resonator, mirrors). The coupled interaction of the laser-beam polarisation and the orientation of the crystal leads to four independent variables: (1) the direction of the laser beam relative to the crystal [e.g., $x(yy)y$, cf. Porto notation in Porto and Krishnan (1967)]; (2) the polarisation of the laser beam relative to the crystal [$y(xy)y$)]; (3) the polarisation of the luminescence emission relative to the crystal [$y(yx)y$], and (4) the direction of luminescence emission detected relative to the crystal [$y(yy)x$]. Most spectrometer systems used in geoscientific research are coupled to microscopes, in which the laser beam and the emission detected proceed in opposite direction through the observing objective lens ($x(yy)\bar{x}$, quasi-backscattering set-up). Hence, the latter variable cannot be analysed separately using such a system set-up. Figure 4 shows the other three aspects with the example of laser-induced photoluminescence spectra of Nd^{3+} ($^4F_{3/2} \rightarrow {}^4I_{9/2}$) in synthetic tetragonal Nd^{3+}:YPO_4 (xenotime structure type, $I4_1/amd$). Please note that the measurement conditions, e.g., laser power, measurement point on the sample, accumulation time etc., were kept strictly identical. Figure 4a demonstrates the effect of a polarised laser beam with the electric field vector (E) aligned along different crystallographic directions; here the laser beam is directed along the crystallographic x axes; the polarisation of the electric field vector is aligned in y and z, respectively. The polarisation of the emission is neglected (no polarisation filters), all intensity of the randomly polarised signal in plane $z - y$ is detected. Changing the polarisation direction of the laser beam causes intensity ratios of the luminescence sublevels to vary significantly. The main sublevel band at 11,467 cm^{-1} is most strongly affected.

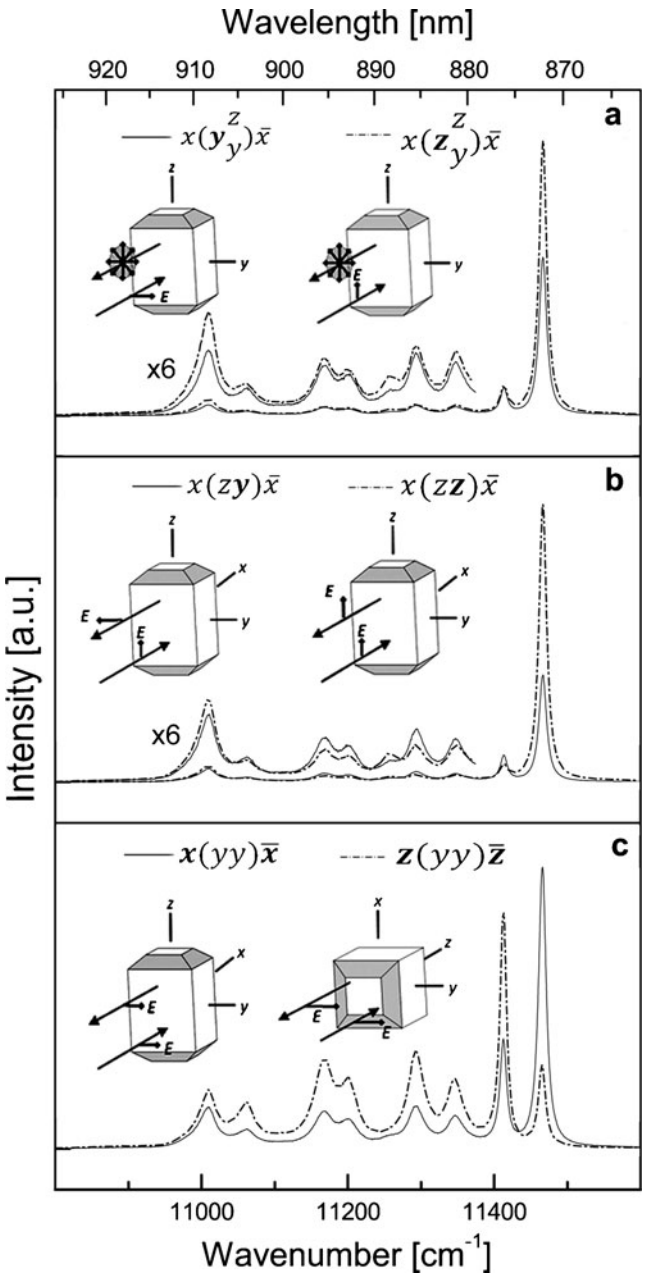

Fig. 4 Orientation-dependence of the laser-induced PL (532 nm excitation) of Nd^{3+} ($^4F_{3/2} \rightarrow {}^4I_{9/2}$) in synthetic tetragonal Nd^{3+}:YPO_4 (xenotime; $I4_1/amd$). Note that all spectra have the same vertical scaling, intensities are therefore directly comparable. **a** Effect of the polarization of the incident laser beam. **b** Effect of the polarization of the luminescence emission. **c** Effect of the direction (relative to the crystal) of the excitation/emission analysed. Small schematic sketches are inserted for better illustration of the Porto notation quoted above

A polarisation filter placed in the emission path-way reveals that the luminescence emission itself is polarised (Fig. 4b). Analysing the luminescence emission with polarisation filters in different directions leads to significant variations of intensity ratios. Turning the sample perpendicular to its tetragonal main axis (z), with the laser polarization direction and the polarization direction of the analysed emission held constant, results in intensity increases in all other sublevel bands relative to the main at 11,467 cm^{-1} (Fig. 4c).

In contrast to laser-induced photoluminescence, the effect of beam polarisation is without significance using an unpolarised electron or ion beam with cathode-/ionoluminescence techniques. The polarisation of the luminescence emission is of importance especially if the signal is analysed with polarisation filters, which is commonly not done in CL measurements. In Fig. 5 the cathodoluminescence spectra of synthetic xenotime–(Y) and zircon crystals are presented. Although the luminescence was excited with an unpolarized electron beam there are significant effects of different analysing directions relative to the crystal. A potential semi-quantitative estimation of trace elements via cathodoluminescence intensity, as for instance applied to apatite, therefore needs a broad range of carefully calibrated conditions, e.g., standard material, system stability, system response (Cesbron et al. 1993; Barbarand and Pagel 2001). Moreover, other effects, e.g., concentration quenching, quenching/sensitizing by other impurities (Kempe and Götze 2002) and, in particular, the analysing direction relative to the crystal, have to be considered (cf. Barbarand and Pagel 2001).

Effects of the real structure on Nd^{3+} luminescence: the example of monazite–(Ce)

Real structure is defined as the entity of deviations from the ideal chemical composition and structure. A common feature

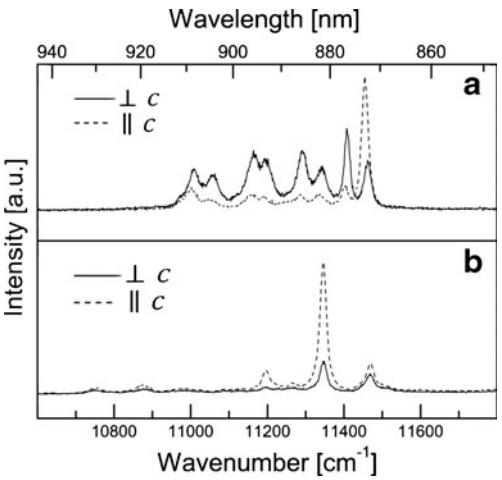

Fig. 5 Orientation dependence of the CL emission of Nd^{3+} ($^4F_{3/2} \rightarrow {}^4I_{9/2}$). **a** Synthetic Nd^{3+}:YPO_4 (xenotime). **b** Synthetic Nd^{3+}:$ZrSiO_4$ (zircon). Note that all spectra have the same vertical scaling, intensities are therefore directly comparable. The emitted CL light was obtained in directions perpendicular and parallel to the *c*-axis of the respective crystal. Note that intensity ratios among sublevel bands vary appreciably

is the presence of defects, including point (e.g., substitutions, vacancies, interstitials), line, or three-dimensional defects (e.g., holes, surface defects, grain boundaries). Typical effects on light-spectroscopic signals are band broadening and shifting. In optical spectroscopy this phenomenon is commonly termed *inhomogeneous broadening* (cf. Macfarlane 1990; cf. Skinner and Moerner 1996). The sharpness of optical transitions, observed either in absorption or emission processes, depends theoretically on the lifetime of the excited electronic state. This is due to the quantum-mechanical uncertainty and includes both radiative and non-radiative processes (Blasse and Grabmaier 1994). For excited states of the f^n configuration, radiative rates are typically in the millisecond and sub-millisecond time scale. This is because these transitions are parity-forbidden and often spin-forbidden as well (Blasse and Grabmaier 1994; Gaft et al. 2001; Liu and Jacquier 2005). At hypothetical ideal conditions, absorption and emission bands of REE have very narrow Lorentzian shapes. These conditions include: REE substituents of the same type with no cross-interaction, a perfect crystal without defects/strain, and without any lattice vibrations (phonons) achieved at very low temperature (ideally 0 K with hypothetically no vibronic coupling). The observed absorption/emission band is considered as superposition of all electronic transitions of a certain number of REE substituents in the area analysed (*homogeneous broadening*, Fig. 6a). However, effects of the real structure (Fig. 6b) perturb the local environment of the REE centre. As a consequence, the crystal field around the REE cations is randomly distorted to a certain amount and electronic transition energies shift slightly. The observed spectral profiles can then be considered as a broad envelope over much narrower homogeneous lines introducing a Gaussian character to the band shape (schematically illustrated in Fig. 6b).

To illustrate the effect of the real structure on REE luminescence, we use the example of chemically induced disorder in monazite–(Ce) for three reasons: First of all, almost all natural monazite-group minerals contain Nd^{3+} and show Nd-luminescence. Second of all, the monazite structure has an extremely broad range of chemical compositions, so that a variety of substitution mechanisms can be studied. Third, Ruschel et al. (2012) have recently studied the structural disorder of monazite–(Ce) using Raman spectroscopy (band broadening of the symmetric stretching vibration of PO_4 tetrahedrons; A_{1g} mode). This was done with the basic objective to investigate, and distinguish among, disturbing effects of the chemical composition and/or structural damage as caused by self-irradiation due to the incorporation of actinide elements. Panczer et al. (2012) showed that the incorporation of non-formula elements affects the sharp sublevel luminescence bands of Nd^{3+} as well. In the present paper we address the question whether Nd^{3+}-luminescence spectroscopy can be used for a quantitative estimation of the chemically induced structural disorder.

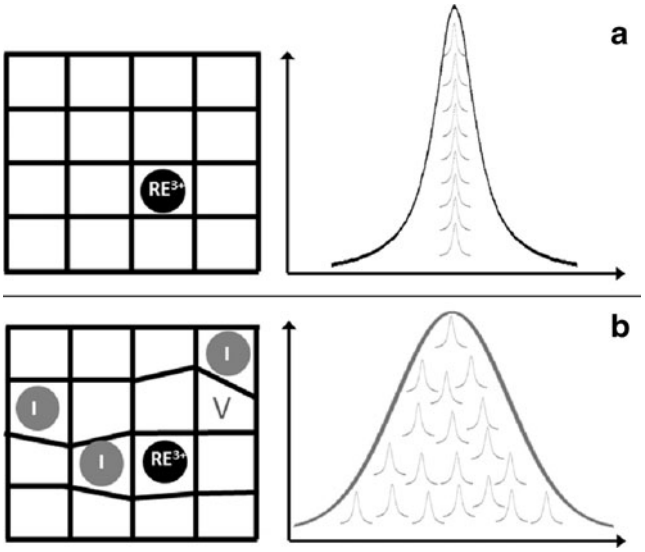

Fig. 6 Schematic illustration (simplified) of the band broadening related to optical transitions as affected by the sample's real structure (modified after Skinner and Moerner 1996). **a** Nearly "ideal" crystal (merely doped with low levels of an individual REE), assuming the absence of notable amounts of defects and strain. The observed absorption or emission band, respectively, is considered as superposition of all electronic transitions of a certain number of REE substituents in the area analysed (*homogenous broadening*). **b** "Real" crystal with notable amounts of defects such as impurities (I), vacancies (V), and non-formula constituents, resulting in notable lattice strain. Here, the crystal field around the REE site is perturbed randomly. The observed spectral profile is a broad envelope over much narrower homogenous lines (*inhomogeneous broadening*)

Monazites are monoclinic orthophosphates with the general formula LREE[PO_4]. These minerals have an extremely broad range of chemical compositions with Ce being the predominant cation in naturally occurring species. Solid solutions with other minerals of the monazite group allow extensive substitutions of Ce by other LREEs (especially La, Nd, Sm). In addition to the more limited incorporation of heavy REEs, significant amounts of the actinide elements Th and U, and to much lesser extent radiogenic Pb, may also be present (Williams et al. 2007). The incorporation of non-REE ions in the wt% range is commonly explained by the two coupled substitutions: (1) $2REE^{3+} \leftrightarrow Ca^{2+} + Th^{4+}$ (*cheralite substitution*) and (2) $P^{5+} + REE^{3+} \leftrightarrow Si^{4+} + Th^{4+}$ (*huttonite substitution*). The continuity in the monazite-huttonite series extends to a maximum of 30 at% huttonite in natural monazites (Della Ventura et al. 1996; Kucha 1980; Förster and Harlov 1999). The substitution mechanisms for Th^{4+} can be applied to U^{4+}, also. For details on the crystal chemistry of the monazite structure the reader is referred to reviews by Kolitsch and Holstam (2004) and Clavier et al. (2011).

Here we present Nd^{3+} luminescence data for three different sample sets reflecting different substitution mechanisms: (1) a series of homogeneous synthetic $Ce_{1-x}LREE_xPO_4$ crystals doped with large amounts of other REEs, forming

a solid solution with LREE = La, Nd, Gd (for detailed characterisation see Ruschel et al. 2012); (2) synthetic samples doped with Th^{4+} compensated with Ca^{2+} and/or Na^{+} (see details in the sample description above); and (3) homogeneous natural monazite–(Ce) samples reflecting combined substitution mechanisms in nature including the huttonite substitution with charge compensation by Si^{4+} on anion-sites (for detailed characterisation see Ruschel et al. 2012).

Figure 7 shows that the exclusive substitution of homovalent REE^{3+} for Ce^{3+} on the cation-site causes only minor band broadening. Monazites–(Ce) with heterovalent substitutions, such as Th^{4+}, Ca^{2+} on cation and Si^{4+} on the anion site, show stronger band broadening and shifting (Fig. 7). In this case, the FWHM (full width at half maximum) of the sublevel bands lowers the probability of a precise deconvolution/fitting due to an effective band overlap. Hence, the less affected out of the eight distinctive sublevel bands at ca. 11,030 abs. cm^{-1} is chosen for the interpretation of the FWHM hereafter.

To describe chemically induced disorder we introduce a *distortion parameter* (Δ) which reflects the distortional behaviour of every substituent on regular cation and anion sites. This is approximated with a summation of the weighted ionic radii difference between the predominant cation/anion (Ce/P in monazite–Ce) and each substituent:

$$\Delta = \sum\nolimits_{cs} c_{cs} * |r_c - r_{cs}| + \sum\nolimits_{as} c_{as} * |r_a - r_{as}| \qquad (1)$$

where c is the concentration of cation (c_{cs}) or anion substituents (c_{as}) in atomic percent per formula unit (apfu), and

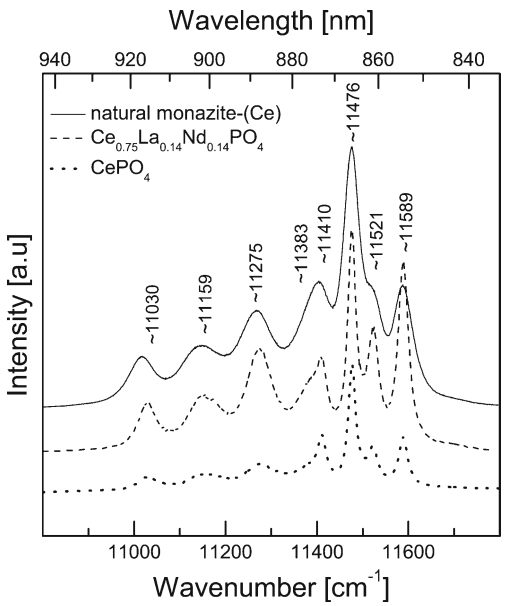

Fig. 7 Photoluminescence spectra (532 nm excitation) of Nd^{3+} ($^4F_{3/2} \rightarrow {}^4I_{9/2}$) of annealed, Th-rich natural monazite-(Ce) from Central Australia (sample ECA6 of Ruschel et al. 2012) in comparison with La,Nd-doped and un-doped $CePO_4$. Band positions are quoted for un-doped $CePO_4$

r the ionic radius of the predominant cation (r_c) or anion (r_a), and of the cation (r_{cs}) or anion substituent (r_{as}), respectively. For monazite–(Ce), the cationic radii in 9-fold and anionic radii of P and Si in 4-fold coordination after Shannon (1976) are used. This formalism takes into account that large ionic radii differences between predominant and substitutional ions should have much more distortional impact than smaller. Additionally, this impact is weighted with the concentration of each ion providing an effective distortional impact which is summed over all substitutional ions present.

Figure 8 shows the effects of chemical substitution on spectral parameters of the Nd^{3+} ($^4F_{3/2} \rightarrow {}^4I_{9/2}$) luminescence emission. An increase of the distortion parameter (Δ), calculated from chemical data of all investigated monazite–(Ce) samples (i.e., Table 2), causes a band shift to lower wavenumbers. In this case, the band shift is linear to the total sum of weighted radii differences of all substituents (Δ). This indicates that the substitution of smaller ions than Ce causes a reduced cell volume. Clavier et al. (2011) summarized data suggesting a complete solid solution in the synthetic system $LaPO_4$–$ThSiO_4$ with linearly decreasing cell parameters with increasing Th content. Alike, unit cell parameters decrease linearly with the substitution ratio in the $La_xGd_{1-x}PO_4$ monazite solid solution (Clavier et al. 2011).

Interestingly, the FWHM of the Nd^{3+}-luminescence bands is mainly controlled by heterovalent substituents (Figs. 7 and 8b). The Δ_{hetero} parameter in Fig. 8b was calculated applying Eq. 1 only to heterovalent substituents present in the samples analysed. The comparison of spectral parameters of the Ce_{1-x} $REE_x[PO_4]$ solid solution (filled triangle, Fig. 8) gives an illustrative example: The extensive substitution of homovalent REE^{3+} causes large band shifts (Fig. 8a), but have no effect on the FWHM (Fig. 8b). Heterovalent substitutions appear to have a much higher impact on the electronic structure and therefore on the perturbation of electronic states than homovalent ones (see the discussion on the crystal field above). Hence, the FWHM of luminescence bands is rather a measure of the perturbed electronic structure which is in this case connected to chemically induced disorder via substitution of heterovalent ions.

The estimation of structural disorder by radii differences applied above is based upon a rigid hard-sphere model of ions and cannot take into account lattice distortion by other real-structure defects, e.g., vacancies. Nevertheless, the good fit to a linear trend suggests that the inferred disorder is mainly controlled by the different chemical substitution mechanisms in the synthetic and natural monazites analysed in this study. Panczer et al. (2012) correlate the FWHM of Nd-luminescence bands of natural monazites with the thorium content (wt%) without regarding other heterovalent substitutions. For comparison, we show a similar correlation of our samples in Fig. 8c. The variance of FWHM among the natural

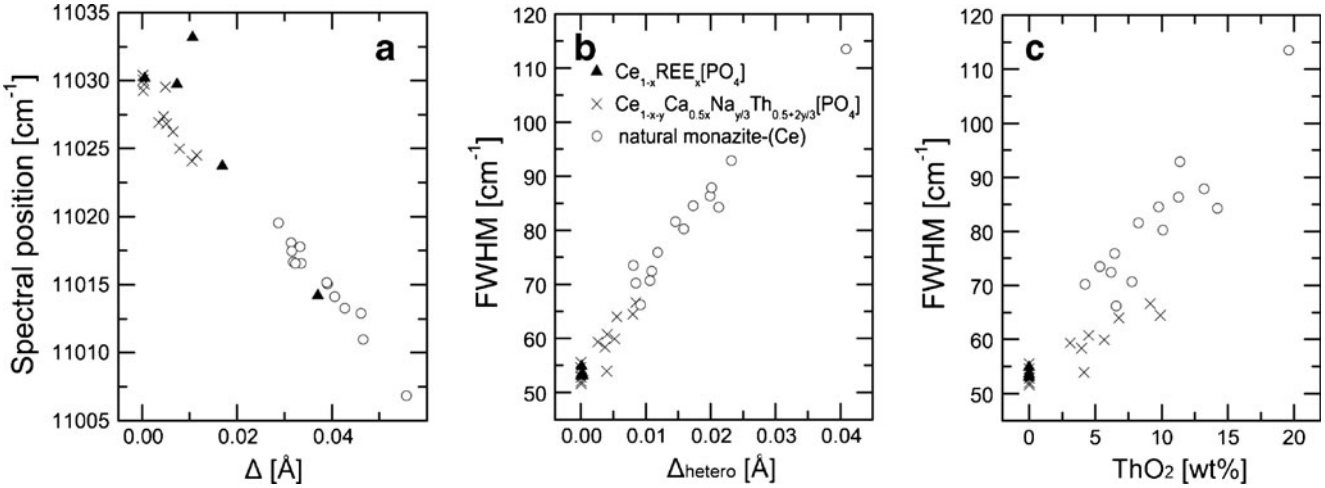

Fig. 8 Effects of chemical substitutions in various natural and synthetic monazite samples on spectral parameters of the Nd^{3+} ($^4F_{3/2} \rightarrow {}^4I_{9/2}$) luminescence emission, shown for the ~11,030 cm^{-1} sublevel band (see Fig. 7). **a** The increase of the distortion parameter Δ (see text and Eq. 1) causes a band shift to lower wavenumbers. **b** The increase of the heterovalent distortion parameter Δ_{hetero} (see text) causes a linear increase of the band FWHM. **c** Band FWHM and ThO_2 content show a less pronounced correlation, making potential estimates of the chemically induced structural disorder from the ThO_2 content alone rather imprecise

samples (open dots) is greater than for the correlation in Fig. 8b. The FWHMs of synthetic multi-doped monazite samples (cross, Fig 8) show an individual correlation with the ThO_2 content. Therefore, the correlation of the FWHM – as potential estimation of structural disorder – with the ThO_2 content alone is imprecise if variable substitution mechanisms determine the chemical composition.

In this study, potential effects of corpuscular self-irradiation on the structural disorder are excluded by using synthetic or annealed samples. The estimation of the chemical impact on the REE-luminescence band widths is of major importance for the discrimination and quantification of irradiation-induced disorder by REE-luminescence spectroscopy (see the review chapter of Nasdala et al. in this special issue). The irradiation-induced disorder accumulated in geologic timescales can be quantified if the chemical-dependent contribution is known. Hence, REE-luminescence spectroscopy may be a complementary technique to Raman spectroscopy, especially for minerals where distinctive Raman bands are absent (e.g., titanite or pyrochlore).

Furthermore, information on the chemically induced structural disorder derived from REE-luminescence data may help to study the dynamics in solid solutions and the interpretation of zoning patterns. This is illustrated in Fig. 9, which presents

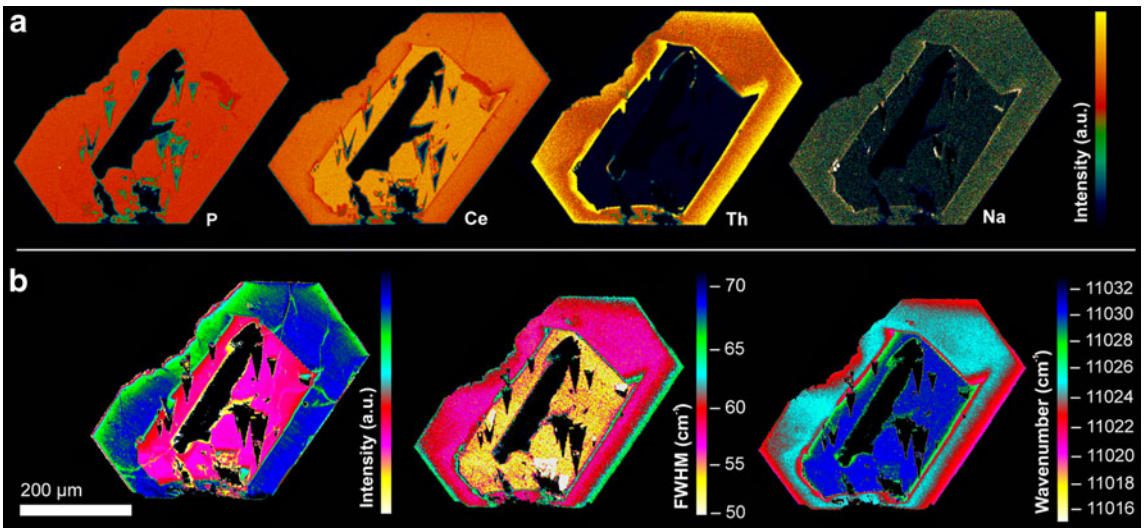

Fig. 9 Element distribution maps (**a**) and hyperspectral Nd^{3+} maps (**b**) of a synthetic Th-doped monazite single crystal. The latter shows distributions of spectral parameters of the ~11,030 cm^{-1} sub-band of the $^4F_{3/2} \rightarrow {}^4I_{9/2}$ electronic transition of Nd^{3+}. Irregularities in the inner zone (i.e. black triangular areas) are flux inclusions and outbreaks from polishing. Note that changes in Nd-luminescence parameters (especially the FWHM) correlate closely with changes in the incorporation of non-formula elements

element distribution (Fig. 9a) and hyperspectral Nd-luminescence maps (Fig. 9b) of a synthetic Th-doped monazite–(Ce). The single crystal shown is characterised by two major zones of significantly different chemical composition. The inner area consists of $CePO_4$ with extremely low amounts of trace elements below the EPMA detection limits, and represents an early stage of crystal growth in the flux. The outer zone (ca. 30–70 μm in width) contains elevated amounts of Th, Ca, and Na and is hence depleted in Ce (average chemical formula $Ce_{0.854}Th_{0.084}\ Ca_{0.039}Na_{0.023}PO_4$). The rim of the crystal (i.e. the outermost ca. 5–10 μm of the outer zone) is strongly enriched in Th. Note that the Th-doped synthetic samples contain well-detectable amounts of Na (Table 2), which we assign to their growth in a sodium-polyphosphate flux (cf. description of synthesis details above). Table 2 presents element quantities (quoted in apfu) of several measurement points on the synthetic Th-doped monazite–(Ce) samples. It was observed for all individual analyses that after subtraction of the respective Th amount related to the cheralite component ($2REE^{3+} \leftrightarrow Ca^{2+} + Th^{4+}$; Ca:Th = 1:1), the ratio of the remaining Na–to–Th is close to 1:2. This suggests a substitution mechanism according to

$$Na^{+} + 2Th^{4+} \leftrightarrow 3Ce^{3+} \quad (2)$$

To the best of our knowledge, this Na–Th substitution has not been described for natural monazite–(Ce) thus far.

The Nd-luminescence parameters are very sensitive to the structural disorder as introduced by the presence of non-formula elements (cf. again Fig. 9b). The FWHM of the ~11,030 cm^{-1} sublevel band broadens from 53 cm^{-1} in the case of nearly pure $CePO_4$ (inner area) up to 65 cm^{-1} near the Th-rich rim of the crystal, accompanied by a shift of the band position from 11,031 cm^{-1} to 11,022 cm^{-1}. In all interior regions and zones, the concentration of Nd was below the EPMA detection sensitivity. We speculate that Nd may be slightly enriched in the outer zone, coupled to the other substituents; this is concluded from the generally higher Nd-luminescence intensity in this area. Other potential causes of lateral differences in the Nd-emission intensity – such as quenching and/or sensitizing (e.g., Marfunin 1979) or effects of structural disorder (e.g., Nasdala et al. 2006) – can be excluded in our case of synthetic, mildly Nd-contaminated specimens.

Temperature dependence

An additional important factor affecting the REE-luminescence band width (and marginally the band position) is temperature. Increasing temperature enhances the extent of lattice vibrations (phonons). Lattice vibrations induce an oscillation of interatomic distances at the luminescence centre within the crystal structure. In consequence, the potential energy of electronic states and thus the transition energy of corresponding optical phenomena are distributed around an equilibrium value. The observed band shape is again a sum of all constituent transitions over a specific time interval in the analysed area. Luminescence measurements are commonly done at very low temperatures to avoid this additional perturbation (vibronic coupling). In general, lowering the temperature allows an improved separation of the obtained luminescence features, but also enables transitions from excited levels, which have previously been depopulated via phonons (non-radiative transitions). The temperature effect on REE band widths is comparatively small compared with *d-d* or *d-f* transitions, where absorption and luminescence band widths are much larger. This is because *f*-electrons and their inter-transitions are well shielded by the outermost filled $5s^2 5p^6$ orbitals, so that the interaction with the ligands is small.

Figure 10 illustrates the effect of temperature on the Nd^{3+} luminescence with the monazite–(Ce) example discussed above: The FWHMs of all the eight observed sublevel bands of the Nd^{3+} ($^4F_{3/2} \rightarrow {}^4I_{9/2}$) emission increase with increasing temperature. The FWHM of broad sublevel bands increases much more than those of the thinner ones (Fig. 10). Similarly, broad bands show the strongest positional shift. However, the shift of the broadest band at 11,159 cm^{-1} does not exceed 9 cm^{-1} (0.7 nm) from 80 K to 300 K. The low sensitivity of the band position to higher temperature is a useful feature for high temperature experiments with diamond anvil cells (DAC), where optical-luminescence pressure-gauges are used successfully. Datchi et al. (1997; 2007) promote the distinct luminescence emission of Sm^{2+} (intra $4f^6$; $^5D_0 \rightarrow {}^7F_0$) doped SrB_4O_7 as viable temperature-

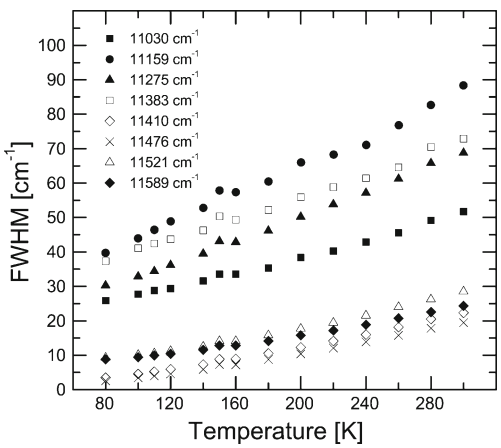

Fig. 10 Effect of temperature on the FWHM of eight distinctive luminescence sublevel bands (Nd^{3+}, $^4F_{3/2} \rightarrow {}^4I_{9/2}$) of synthetic $CePO_4$. Temperature increase causes general broadening of sublevel bands, with broader bands showing stronger absolute increase of their FWHM, compared to narrower bands

insensitive alternative to the Cr^{3+} (R-lines) luminescence of ruby (Cr^{3+}:Al_2O_3).

The prediction of FWHMs and shifts of REE bands cannot be deduced from first principles. The temperature not only affects the electronic interaction within the luminescent REE^{3+} ion, but also the surrounding ligands of the crystal field. An anisotropic thermal expansion of the crystal structure stresses the cation site (Mogilevsky et al. 2007; Jardin et al. 2008; Li et al. 2009) and results in a anisotropic crystal field splitting, which is further influenced by local defects. This consideration is of crucial importance for the evaluation of band widths for the quantification of chemically induced (see above) or radiation-induced disorder (see the review chapter of Nasdala et al. in this special issue). Figure 11 shows the FWHM of the 11,030 cm^{-1} Nd-sublevel band of different monazite–(Ce) samples with various chemical compositions. Chemically induced disorder not only causes higher FWHMs but also influences the impact of the temperature effect. High chemical disorder inhibits the effect of temperature broadening, possibly due to structural relaxation induced by the presence of non-formula elements. Measuring the FWHMs for the quantification of e.g., chemically induced disorder gives different absolute values at different temperatures, whereby the relative significance is not changed drastically. Hence, an absolute FWHM correlation with effects connected to structural disorder should be done at constant temperature, which is done throughout this study. All luminescence spectra presented in the sections above are recorded at room temperature (298 K), because low temperature measurements using cooling stages or other liquid-nitrogen set-ups entail considerable effort; especially for measurements with high lateral resolution for hyperspectral luminescence maps (cf. Fig. 9).

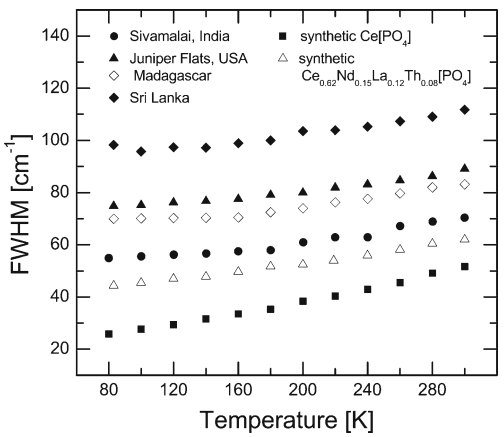

Fig. 11 Influence of the chemical composition on the FWHM-temperature dependence, for the example of the ~11,030 cm^{-1} Nd^{3+} sublevel. Chemically induced disorder not only causes FWHM increases (cf. Fig. 8a) but also decreases the effect of temperature on the band broadening, possibly due to structural relaxation by the substituents

Concluding remarks

First of all, the luminescence emission of REE^{3+} in minerals depends on the type of incorporated REEs. The energetic positions of their spectroscopic levels determine the luminescence emission pattern (a chart of spectroscopic levels of all REE^{3+} was given by Carnall et al. 1989). Commonly, natural samples contain more than one type of REE^{3+}, often resulting in extensively overlapping luminescence patterns. Due to electronic shielding of the outermost $5s^2$ and $5p^6$ orbitals, the influence on the $4f$ transitions of the crystal field is weak and a specific optical transition of a REE^{3+} appears with comparable spectral energies in very different mineral hosts (Fig. 2). Nevertheless, the crystal field splits spectroscopic levels into sublevels depending on the distribution of the electron density at the substituted lattice site (Fig. 2). Luminescence investigations of REE^{3+} in minerals hence provide first the opportunity to identify REEs in a specific host mineral. Second, they enable fast mineral identification, provided the individual sublevel splitting of a specific REE^{3+} in the mineral under investigation is known. With respect to the latter, the luminescence emission of Nd^{3+} was found to be a promising candidate because (1) the luminescence signal can be traced with standard Si-based detectors, (2) it is effectively excited by standard lasers as well as via cathodoluminescence, (3) other luminescence emissions in the respective spectral energy range are rare, and (4) a low number of sublevels simplifies the data reduction (i.e., fitting/deconvolution).

Even minute amounts of REE^{3+} cause detectable luminescence signals and can potentially be used for the qualitative identification of trace REEs. In contrast to optical absorption spectroscopy, the quantitative estimation of REEs concentrations via luminescence intensity is difficult for several reasons (see detailed discussions above). In particular, this study shows once more that the relative luminescence intensity of certain sublevels may depend strongly on the crystal orientation (Fig. 4). Furthermore, both the polarisation of the incident laser (in the case of laser-induced photoluminescence) and the polarisation of the luminescence signal are of importance when comparing relative luminescence intensities.

The FWHM of REE^{3+} luminescence sublevel bands contains information on the crystal-structural state and provides great opportunities to study different types of structural disorder with luminescence techniques (Fig. 9). In this study, the effect of chemically induced disorder on the luminescence signal of monazite–(Ce) has been described with a simple model based on ionic radii. The discrimination between chemically induced (Fig. 8) and irradiation-induced structural disorder is possible, however, when the influence of measurement temperature (Fig. 10 and 11) is considered.

Acknowledgements We are indebted to U. Kolitsch and G. Giester for providing standard material for comparison purposes. Sample preparation was done by A. Wagner. The lead author is most grateful to M. Wildner for fruitful discussions. Constructive comments by D. Ohnenstetter, M. Gaft and an anonymous reviewer are gratefully acknowledged. Funding of this research was provided by the Austrian Science Fund (FWF) through grant P24448–N19 to LN, and the European Commission through project CZ.1.07/2.3.00/20.0052 "Research group for radioactive waste repository and nuclear safety" to DT and RS.

References

Barbarand J, Pagel M (2001) Cathodoluminescence study of apatite crystals. Am Mineral 86:473–484

Belsky A, Krupa J (1999) Luminescence excitation mechanisms of rare earth doped phosphors in the VUV range. Displays 19:185–196

Blanc P, Baumer A, Cesbron F, Ohnenstetter D, Panczer G, Rémond G (2000) Systematic cathodoluminescence spectral analysis of synthetic doped minerals: anhydrite, apatite, calcite, fluorite, scheelite and zircon. In: Pagel M, Barbin V, Blanc P, Ohnstetter D (eds) Cathodoluminescence in geosciences. Springer, Berlin, pp 127–160

Blasse G, Grabmaier B (1994) Luminescence materials. Springer, Berlin, 248 p

Boatner LA (2002) Synthesis, structure, and properties of monazite, pretulite, and xenotime. Rev Mineral Geochem 48:87–121

Bünzli JCG, Piguet C (2005) Taking advantage of luminescent lanthanide ions. Chem Soc Rev 34:1048–1077

Burns RG (1993) Mineralogical applications of crystal field theory, Cambridge University Press

Carnall W, Goodman G, Rajnak K, Rana R (1989) A systematic analysis of the spectra of the lanthanides doped into single crystal LaF. J Chem Phys 90:3443–3457

Cesbron F, Ohnenstetter D, Blanc P, Rouer O, Sichere MC (1993) In corporation des terres rares dans des zircons de synthèse: étude par cathodoluminescence. C R Acad Sci II 316:1231–1238

Cesbron F, Blanc P, Ohnenstetter D, Rémond G (1995) Cathodoluminescence of rare earth doped zircons. I. Their possible use as reference materials. Scanning Microscopy Suppl 9:35–56

Clavier N, Podor R, Dacheux N (2011) Crystal chemistry of the monazite structure. J Eur Ceram Soc 31:941–976

Czaja M, Bodył S, Głuchowski P, Mazurak Z, Strek W (2008) Luminescence properties of rare earth ions in fluorite, apatite and scheelite minerals. J Alloy Compd 451:290–292

Czaja M, Bodył S, Lisiecki R, Mazurak Z (2009) Luminescence properties of Pr^{3+} and Sm^{3+} ions in natural apatites. Phys Chem Miner 37:425–433

Datchi F, LeToullec R, Loubeyre P (1997) Improved calibration of the SrB4O7:Sm2+ optical pressure gauge: advantages at very high pressures and high temperatures. J Appl Phys 81:3333–3339

Datchi F, Dewaele A, Loubeyre P, Letoullec R, Le Godec Y, Canny B (2007) Optical pressure sensors for high-pressure–high-temperature studies in a diamond anvil cell. High Press Res 27:447–463

Della Ventura G, Mottana A, Parodi GC, Raudsepp M, Bellatreccia F, Caprilli E, Rossi P, Fiori S (1996) Monazite-huttonite solid-solutions from the vico volcanic complex, Latium, Italy. Mineral Mag 60:751–758

Dexpert-Ghys J, Faucher M, Caro P (1984) Site selective spectroscopy and structural analysis of yttria-doped zirconias. J Solid State Chem 54:179–192

Dexpert-Ghys J, Mauricot R, Faucher M (1996) Spectroscopy of Eu^{3+} ions in monazite type lanthanide orthophosphates $LnPO_4$, Ln= La or Eu. J Lumin 69:203–215

Finch A, Hole D, Townsend P (2003) Orientation dependence of luminescence in plagioclase. Phys Chem Miner 30:373–381

Förster H, Harlov D (1999) Monazite–(Ce)-huttonite solid solutions in granulite-facies Metabasites from the Ivrea-Verbano Zone, Italy. Mineral Mag 63:587–594

Friis H, Finch AA, Williams CT, Hanchar JM (2009) Photoluminescence of zircon (ZrSiO4) doped with REE^{3+} (REE = Pr, Sm, Eu, Gd, Dy, Ho, Er). Phys Chem Miner 37:333–342

Gaft M, Reisfeld R, Panczer G, Shoval S, Champagnon B, Boulon G (1997) Eu^{3+} Luminescence in high-symmetry sites of natural apatite. J Lumin 72:572–574

Gaft M, Reisfeld R, Panczer G, Uspensky E, Varrel B, Boulon G (1999) Luminescence of Pr^{3+} in minerals. Opt Mater 13:71–79

Gaft M, Panczer G, Reisfeld R, Uspensky E (2001) Laser-induced time-resolved luminescence as a tool for rare-earth element identification in minerals. Phys Chem Miner 28:347–363

Gaft M, Reisfeld R, Panczer G (2005) Luminescence spectroscopy of minerals and materials. Springer, Berlin, 372 p

Götze J (2000) Cathodoluminescence microscopy and spectroscopy in applied mineralogy. Freiberger Forschungsheft C 485, TU Bergakademie Freiberg, 128 p

Götze J (2002) Potential of cathodoluminescence (CL) microscopy and spectroscopy for the analysis of minerals and materials. Anal Bioanal Chem 374:703–708

Götze J, Habermann D, Neuser RD, Richter DK (1999) High-resolution spectrometric analysis of rare earth elements-activated cathodoluminescence in feldspar minerals. Chem Geol 153:81–91

Habermann D (2002) Quantitative cathodoluminescence (CL) spectroscopy of minerals: possibilities and limitations. Miner Petrol 76:247–259

Habermann D, Neuser RD, Richter DK (1996) REE-activated cathodoluminescence of calcite and dolomite: high-resolution spectrometric analysis of CL emission (HRS-CL). Sediment Geol 101:1–7

Hanchar J, Miller C (1993) Zircon zonation patterns as revealed by cathodoluminescence and backscattered electron images: implications for interpretation of complex crustal histories. Chem Geol 110:1–13

Hanchar J, Rudnick R (1995) Revealing hidden structures: the application of cathodoluminescence and back-scattered electron imaging to dating zircons from lower crustal xenoliths. Lithos 36:289–303

Hanchar JM, Finch RJ, Hoskin PWO, Watson EB, Cherniak DJ, Mariano AN (2001) Rare earth elements in synthetic zircon: part 1. Synthesis, and rare earth element and phosphorus doping. Am Mineral 86:667–680

Jardin R, Pavel CC, Raison PE, Bouëxière D, Santa-Cruz H, Konings RJM, Popa K (2008) The high-temperature behaviour of $PuPO_4$ monazite and some other related compounds. J Nucl Mater 378:167–171

Kempe U, Götze J (2002) Cathodoluminescence (CL) behaviour and crystal chemistry of apatite from rare-metal deposits. Mineral Mag 66:151–172

Kenyon A (2002) Recent developments in rare-earth doped materials for optoelectronics. Prog Quant Electron 26:225–284

Kolitsch U, Holtstam D (2004) Crystal chemistry of $REEXO_4$ compounds (X= P, as, V). II. Review of $REEXO_4$ compounds and their stability fields. Eur J Mineral 16:117–126

Kucha H (1980) Continuity in the monazite-huttonite series. Mineral Mag 43:1031–1034

Li H, Zhang S, Zhou S, Cao X (2009) Bonding characteristics, thermal expansibility, and compressibility of RXO_4 (R = rare earths, X = P, as) within monazite and zircon structures. Inorg Chem 48:4542–4548

Liu G, Jacquier B (2005) Spectroscopic properties of rare earths in optical materials. Springer, Berlin, 550 p

Macfarlane R (1990) Inhomogeneous broadening of spectral lines in doped insulators. J Lumin 45:1–5

MacRae CM, Wilson NC, Johnson SA, Phillips PL, Otsuki M (2005) Hyperspectral mapping –combining cathodoluminescence and X-ray collection in an electron microprobe. Microsc Res Techniq 67:271–277

MacRea CM, Wilson NC, Torpy A, Davidson CJ (2012) Hyperspectral cathodoluminescence imaging and analysis extending from ultra-violet to near infrared. Microsc Microanal 18:1239–1245

Marfunin AS (1979) Spectroscopy, Luminescence, and Radiation Centers in Minerals. Springer, Berlin Heidelberg, New York, p 352

Mogilevsky P, Boakye E, Hay R (2007) Solid solubility and thermal expansion in a $LaPO_4$-YPO_4 system. J Am Ceram Soc 90:1899–1907

Nasdala L, Götze J, Hanchar J, Gaft M, Krbetschek M (2004) Luminescence techniques in earth sciences. In: Beran A, Libowitzky E (eds) Spectroscopic methods in mineralogy, vol 6, Eur mineral union notes in mineralogy. Eötvös Univ Press, Budapest, pp 43–91

Nasdala L, Kronz A, Hanchar JM, Tichomirova M, Davis DW, Hofmeister W (2006) Effects of natural radiation damage on back-scattered electron images of single crystals of minerals. Am Mineral 91:1739–1746

Neuser R, Bruhn F, Götze J, Habermann D, Richter D (1995) Kathodolumineszenz: methodik und anwendung. Zbl Geo Pal I 1995(1/2):287–306

Ohnenstetter D, Cesbron F, Rémond G, Caruba R, Claude JM (1991) Emission de cathodoluminescence de deux populations de zircons naturels: tentative d'interprétation. C R Acad Sci II 313:641–647

Ollier N, Concas G, Panczer G, Champagnon B, Charpentier T (2003) Structural features of a Eu^{3+} doped nuclear glass and gels obtained from glass leaching. J Non-Cryst Solids 328:207–214

Owen JJ, Cheetham AK, McFarlane RA (1998) Orientation-dependent fluorescence studies and spectroscopic analysis of doped barium yttrium fluoride upconversion laser crystals ($BaY_{2-x-y}Yb_xTm_yF_8$). J Opt Soc Am B 15:684–693

Panczer G, De Ligny D, Mendoza C, Gaft M, Sexdoux-Guillaume A, Wang X (2012) Raman and fluorescence. In: Dubessy J, Caumon M-C, Rull F (eds) Applications of Raman spectroscopy to Earth sciences and cultural heritage. Eur Mineral Union Notes in Mineralogy, vol 12. Eur Mineral Union and Mineral Soc of Great Britain and Ireland, pp 61–82

Piriou B, Elfakir A, Quarton M (2001) Site-selective spectroscopy of Eu^{3+}-doped sodium lead phosphate apatite. J Lumin 93:17–26

Porto S, Krishnan R (1967) Raman effect of corundum. J Chem Phys 47:1009–1013

Pouchou J-L, Pichoir F (1991) Quantitative analysis of homogeneous or stratified microvolumes applying the method "PAP". In: Heinrich KFJ, Newbury DE (eds) Electron probe quantitation. Plenum Press, New York, pp 31–75

Rakovan J, Reeder RJ (1996) Intracrystalline rare earth element distributions in apatite: surface structural influences on incorporation during growth. Geochim Cosmochim Ac 60:4435–4445

Reisfeld R (2005) Spectroscopy of rare earth ions. In: Vaseashta A, Dimova-Malinovska D, Marshall JM (eds) Nanostructured and advanced materials for applications in sensor, optoelectronic and photovoltaic technology, Nato Sci Ser II math, vol 204. Springer, Berlin, pp 77–100

Reisfeld R, Gaft M, Boulon G, Panczer C, Jørgensen C (1996) Laser-induced luminescence of rare-earth elements in natural fluor-apatites. J Lumin 69:343–353

Reisfeld R, Zigansky E, Gaft M (2004) Europium probe for estimation of site symmetry in glass films, glasses and crystals. Mol Phys 102:1319–1330

Richter D, Götte T, Götze J, Neuser R (2003) Progress in application of cathodoluminescence (CL) in sedimentary petrology. Miner Petrol 79:127–166

Richter D, Gorgen P, Götte T (2008) Monazite cathodoluminescence – a new tool for heavy mineral analysis of siliciclastic sedimentary rocks. Sediment Geol 209:36–41

Ruschel K, Nasdala L, Kronz A, Hanchar JM, Többens DM, Škoda R, Finger F, Möller A (2012) A Raman spectroscopic study on the structural disorder of monazite–(Ce). Miner Petrol 105:41–55

Seydoux-Guillaume AM, Wirth R, Nasdala L, Gottschalk M, Montel JM, Heinrich W (2002) An XRD, TEM and Raman study of experimentally annealed natural monazite. Phys Chem Miner 29:240–253

Shannon R (1976) Revised effective ionic radii and systematic studies of interatomic distances in halides and chalcogenides. Acta Crystallogr A 32:751–767

Skinner J, Moerner W (1996) Structure and dynamics in solids as probed by optical spectroscopy. J Phys Chem 100:13251–13262

Talla D, Beran A, Škoda R, Losos Z (2011) On the presence of OH defects in the zircon-type phosphate mineral xenotime, (Y, REE)PO_4. Am Mineral 96:1799–1808

Tarashchan AN (1978) Luminescence of minerals. Naukova Dumka, Kiev, 296 p (in Russian)

Ternane R, Ferid M, Panczer G, Trabelsi-Ayadi M, Boulon G (2005) Site-selective spectroscopy of Eu^{3+}-doped orthorhombic lanthanum and monoclinic yttrium polyphosphates. Opt Mater 27:1832–1838

Waychunas GA (2002) Apatite luminescence. In: Kohn ML, Rakovan J and Hughes JM (eds) Rev Mineral Geochem, vol 48. Mineral Soc Am, Washington DC, 701–742

Williams ML, Jercinovic MJ, Hetherington CJ (2007) Microprobe monazite geochronology: understanding geologic processes by integrating composition and chronology. Annu Rev Earth Planet Sci 35:137–175